Passive Wall Tracking for a Rotorcraft with Tilted and Ducted Propellers using Proximity Effects

Runze Ding[1], Yi-Hsuan Hsiao[2], Huaiyuan Jia[1], Songnan Bai[1], and Pakpong Chirarattananon[1]

Abstract—The letter proposes a passive wall following strategy for a multirotor robot based on the aerodynamic interaction between the propeller wake and the vertical surface. To reinforce the proximity effects, a vehicle with tilted and ducted propellers is introduced. Momentum theory is employed to elucidate the changes in horizontal and vertical components of the propelling thrust in the vicinity of a wall. The modeling and force measurements, when combined with the analysis of the flight dynamics, reveal the existence of a stable distance between the robot and a wall when only the attitude and altitude of the robot are controlled. Flight experiments were conducted to validate that the stable distance between the robot and the wall can be manipulated through the attitude setpoint or control gain, eliminating the need for position feedback. The outcomes enable a human operator to effortlessly fly the robot safely along a corridor without a collision in the absence of vision or other sensing instruments.

Index Terms—Aerial Systems: Mechanics and Control, Aerial Systems: Perception and Autonomy, Collision Avoidance, Dynamics, Autonomous Vehicle Navigation

I. Introduction

Multirotor vehicles have demonstrated great potential for applications in urban areas as well as hazardous and inaccessible locations, such as collapsed buildings, forests, caves, and underground mines [1], [2]. This has driven the associated developments in perception [3] and localization and mapping [4]–[6]. Despite such efforts, the challenges of autonomous navigation, when coupled with complexity caused by unstructured environments, means flying robots remain vulnerable to accidental collisions. Impact resilient structures, as a consequence, emerge as a complementary solution to the collision avoidance problem. In the pioneering work [7], the mechanism-based method was presented in the form of an enclosing gimbal system that is mechanically decoupled from the robot. Upon a collision, the gimbal significantly dampens the destabilizing torque on the vehicle. Thus far, other cage-like structures with shared working principles have also been developed [8]–[10]. More recently, the impact mitigating
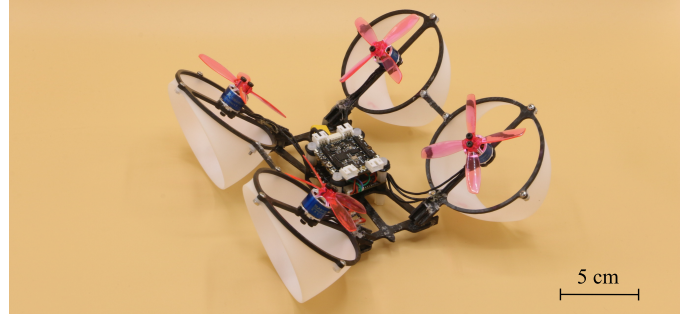
Fig. 1: Photograph of the robot with tilted propellers and custom-made ducts.

component is tightly unified into the airframes [11]–[13]. The integration reduces the footprint of the robots, enhancing their mobility in cluttered environments. While showing great promises, these developments are still in infancy.

In this letter, we simultaneously consider the obstacle detection and collision problems of aerial vehicles. The proposed aerodynamics-based framework permits the multirotor robot shown in Fig. 1 to safely maneuver closely and along a wall without the need for vision or other sensing capabilities while the possibility of a destructive impact is markedly reduced. This is accomplished through the interaction of the wake generated by the tilted propellers and the nearby surface, also known as the proximity effects [14], [15], instead of vision-based and/or mechanical methods previously mentioned.

To date, the subject of the influences of the aerodynamic phenomena has been investigated in the context of small rotorcraft as ground [16], [17], ceiling [18], [19], and, wall [14], [15], [20] effects. These studies primarily report noticeable changes in the propelling forces of small aerial vehicles attributed to nearby surfaces. With pressure sensors [20], [21] or a Kalman-based external wrench estimator [15], it becomes possible to detect and estimate the distance to a nearby surface. The obtained feedback can then be incorporated for position control in order to realize a collision-free flight [21].

Compared to existing solutions, this work proposes a more integrative approach for near-wall navigation and collision mitigation. Unlike a conventional multirotor robot, we first consider a robot with tilted and ducted propellers (Fig. 1) to reinforce the wake-surface interactions. Through momentum theory (MT) analysis and measurements, we show that the design brings about dramatic changes in the propelling force when the robot operates near a vertical surface. The findings are then incorporated into the modeling of closed-loop flight dynamics. The outcome reveals that, without a position controller, there exists an equilibrium, small but nonzero distance between the vehicle and the wall. This implies

the robot is effectively repelled from or attracted towards the wall depending on its relative position. This passively allows the robot to stay close to the surface without a forceful or destructive collision. The flight results support the model predictions, enabling a human operator to fly the robot along the wall with ease as the robot-wall distance is passively stabilized without direct feedback.

All in all, this letter proposes a small rotorcraft with a customized configuration for amplifying the wake interaction with a vertical surface. Through modeling of aerodynamics and flight dynamics, the aircraft is shown capable of passively tracking a wall without visual feedback or additional estimation schemes. The reliance on the surface-flow interaction to passively aid the navigation instead of active detection and avoidance can be regarded as the use of physical intelligence [22] deliberately divised through the vehicle design. The remains of the paper are organized as follows. Section II describes the aerodynamic model of the proximity effect in the context of the proposed robot. The corresponding force and power measurements from a benchtop setup are presented in Section III for the model validation. Section IV details the configuration of the proposed vehicle and its force and torque outputs. In Section V, we show that a simple attitude controller would enable the robot to stabilize next to a wall, with the equilibrium position dependent on the attitude setpoint. Flight experiments are presented in Section VI to validate the proposed passive near-wall position control strategy.

II. PROXIMITY EFFECT OF TILTED AND DUCTED ROTOR

In order to predict how the magnitude and direction of the thrust generated by a spinning propeller is influenced by a nearby wall, we model the aerodynamic performance of a ducted propeller in the vicinity of a vertical surface, primarily to evaluate the change in the propelling thrust in comparison to an isolated propeller. The studied configuration is later adopted for the proposed multirotor vehicle featured in Fig. 1.

A. Tilted and Ducted Propeller

Unlike the nominal condition for a propeller in a conventional multirotor aircraft, the axis of the propeller of interest is angled from the vertical by θ_p. In addition, the propeller, with the radius R, is fitted with a customized duct to manipulate the downstream wake as illustrated in Fig. 2. The cross-section of the duct is marginally larger than the area swept by the propeller, hence, it is assumed to also have the radius R. The opening is normal to the propeller's axis and the profile of the duct is constructed by partially revolving the circular cross-section about the axis tangent to the circle for θ_d, making it a radially sliced horn torus. As a result, the terminal face of the duct makes an angle $\theta_p + \theta_d$ to the vertical as seen in Fig. 2.

Next, to predict the relationship between the propelling thrust and aerodynamic power, momentum theory (MT) is applied. Modifications from the standard actuator disk theory are required to account for the duct and the nearby surface.

B. Momentum Theory Analysis

We hypothesize that the presence of the duct and a vertical surface at the distance d from the tip of the duct substantially
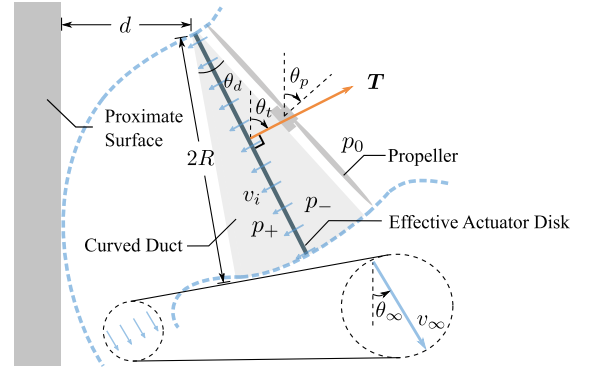

Fig. 2: Momentum theory analysis of a ducted and tilted propeller located next to a vertical surface. The spinning propeller tilts by the angle θ_p from the vertical, generating the thrust $\boldsymbol{T}$ at the angle θ_t from the vertical. The effective propeller disk lies within the duct.

influences the propeller wake. For the MT analysis commonly used for aerodynamic modeling of rotors, the flow is usually assumed quasi-steady, incompressible, inviscid, irrotational, and axisymmetric [18], [23]. In addition, three major suppositions are introduced. First, the infinitesimally thin *effective* propeller disk may no longer coincide with the propeller's plane, but it resides in the duct as depicted in Fig. 2. As a result, the thrust vector $\boldsymbol{T}$ (perpendicular to the effective propeller disk) is not necessarily parallel to the axis of the propeller. Hence, the angle between $\boldsymbol{T}$ and the vertical θ_t may be different from θ_p as $\theta_t \in [\theta_p, \theta_p + \theta_d]$. Second, due to the interaction with the surface, the direction of the air far downstream may not be normal to the propeller disk and is assumed to be θ_∞ from the vertical as illustrated in Fig. 2. Third, the drag induced by the surface is negligible and the energy is still conserved.

To begin, we let p_0 be the atmospheric pressure of the free-stream quiescent air. The effective propeller disk gives rise to a discontinuity in the pressure immediately above (p_-) and below (p_+) the disk, resulting in the thrust $T = (p_+ - p_-)A$ when $A = \pi R^2$. Assuming v_i is the uniform flow speed across the propeller disk, the application of Bernoulli equation along the streamline of the upstream wake yields

$$p_0 = p_- + (1/2)\rho v_i^2, \tag{1}$$

where ρ is the air density. Similarly, the downstream wake is characterized by (since the energy is conserved)

$$p_+ + (1/2)\rho v_i^2 = p_0 + (1/2)\rho v_\infty^2, \tag{2}$$

where v_∞ is the terminal flow velocity far downstream. Subtracting Eq. (1) from (2) and substituting in the pressure difference as $(p_+ - p_-)A = T$ produces

$$T = (1/2)\rho A v_\infty^2, \tag{3}$$

or $v_\infty = \sqrt{2T/\rho A}$. To relate v_i to T, we consider the conservation of momentum along the vertical axis. The difference in the vertical momentum of the incoming and outgoing air is $\rho A v_i v_\infty \cos\theta_\infty$. Neglecting the skin friction drag from the proximate surface, this is equated to the vertical component of the thrust as

$$\rho A v_i v_\infty \cos\theta_\infty = T \cos\theta_t. \tag{4}$$

That is

$$v_i = \frac{T\cos\theta_t}{\rho A v_\infty \cos\theta_\infty} = \sqrt{\frac{T}{2\rho A}} \cdot \frac{\cos\theta_t}{\cos\theta_\infty}. \tag{5}$$

Lastly, we obtain the aerodynamic power contributed by the spinning propeller as

$$P_a = Tv_i = T\sqrt{\frac{T}{2\rho A}} \cdot \frac{\cos\theta_t}{\cos\theta_\infty}. \tag{6}$$

Notice that without the duct and nearby surface, one anticipates the thrust to align with the propeller's axis and the terminal flow direction or $\theta_t = \theta_p = -\theta_\infty$. In that case, the result in Eq. (6) simplifies to $P_a = T\sqrt{T}/\sqrt{2\rho A}$, matching the outcome of the classical MT [23].

C. Thrust Components and Coefficients

In the context of a multirotor robot, quantities of interest are the horizontal and vertical components of the thrust in the robot's frame: $T_h = T\sin\theta_t$ and $T_v = T\cos\theta_t$. They can be deduced from Eq. (6) as

$$T_h = \sin\theta_t \frac{\cos^{\frac{2}{3}}\theta_\infty}{\cos^{\frac{2}{3}}\theta_t} \cdot \left(\sqrt{2\rho A P_a}\right)^{\frac{2}{3}} = \gamma_h \left(\sqrt{2\rho A P_a}\right)^{\frac{2}{3}},$$

$$T_v = \cos^{\frac{1}{3}}\theta_t \cos^{\frac{2}{3}}\theta_\infty \cdot \left(\sqrt{2\rho A P_a}\right)^{\frac{2}{3}} = \gamma_v \left(\sqrt{2\rho A P_a}\right)^{\frac{2}{3}},$$
$$\tag{7}$$

where we have defined the coefficients of proximity effects γ_h, γ_v to capture the effects of the duct and the surface. For a particular propeller at a fixed orientation θ_p, it is reasonable to expect θ_t and θ_∞ to be dependent on the distance to the wall d. Adopting the normalized distance $\bar{d} = d/R$, we may regard $\gamma_h(\theta_t, \theta_\infty) = \gamma_h(\bar{d})$ and $\gamma_v(\theta_t, \theta_\infty) = \gamma_v(\bar{d})$. As a consequence, the relationship between the aerodynamic power and thrust components are captured by γ_h and γ_v.

D. Powers and Motor Commands

To use the findings from Eq. (7) in the context of aerial robots, the aerodynamic power P_a cannot be directly measured. The more relevant quantity is the electrical power P_e. To relate them, we first consider the mechanical power P_m of the spinning propeller, which differs from P_a depending on the aerodynamic efficiency of the propeller by an approximately constant factor known as the figure of merit $\epsilon \in (0, 1)$ as $P_a = \epsilon P_m$. The mechanical power is also lower than the motor's input power P_e due to the resistive loss, but there exists a one-to-one mapping between P_e and P_m as elaborated in [18]. This implies a one-to-one map between P_e and P_a (independent of the proximity effects).

To emphasize the practical effects of a wall on a multirotor vehicle, we consider a robot actuated by brushless DC motors via electronic speed controllers (ESCs). The ESC directly regulates the electrical power such that both P_e and P_a remain constant for a particular driving command. Hence, by letting T_0 and θ_0 be the magnitude and angle of the propelling thrust when the surface is far away such that $T_h(\bar{d} = \infty) = T_0\sin\theta_0$ and $T_v(\bar{d} = \infty) = T_0\cos\theta_0$, Eq. (7) can be normalized as

$$T_h = \bar{\gamma}_h(\bar{d})T_0\sin\theta_0, \quad \text{and} \quad T_v = \bar{\gamma}_v(\bar{d})T_0\cos\theta_0, \tag{8}$$
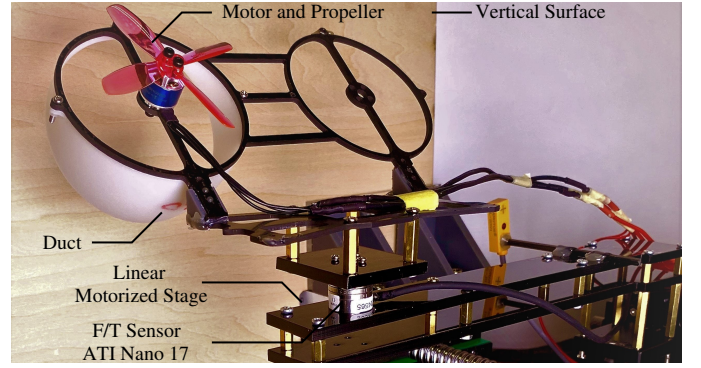

Fig. 3: The platform for propelling force measurement. The ducted propeller is affixed on the load cell, mounted on a motorized stage. This allows the force and power of the propeller to be measured at different driving commands and distances from the vertical surface.

where

$$\bar{\gamma}_h(\bar{d}) = \frac{\gamma_h(\bar{d})}{\gamma_h(\bar{d} = \infty)} \quad \text{and} \quad \bar{\gamma}_v(\bar{d}) = \frac{\gamma_v(\bar{d})}{\gamma_v(\bar{d} = \infty)}, \tag{9}$$

such that both $\bar{\gamma}_h$ and $\bar{\gamma}_v$ are unity when the wall is absent.

The analysis implies that, by controlling the electrical power of the motor-driven propeller, the nominal thrust T_0 is indirectly controlled (Eq. (7)). The actual force components, however, are affected by the proximity to the surface as captured by Eq. (8).

III. BENCHTOP CHARACTERIZATION OF THE PROXIMITY EFFECTS

To empirically evaluate the proximity coefficients (γ_h, γ_v) defined by Eq. (7), a benchtop setup shown in Fig. 3 was employed to measure the propelling thrust and electrical power of a ducted propeller under various operating conditions.

A. Experimental Setup and Procedures

The setup resembles the situation considered by the MT analysis in Section II. A single 4-blade propeller with $R = 32$ mm (LDARC, 2535) and a brushless DC motor (Sunnysky, R1106 8000KV) were mounted at the angle $\theta_p = 45°$. It was fitted with a 3D-printed duct with $\theta_d = 30°$ as depicted in Fig. 3. The components were attached on top of a multi-axis force/torque sensor (ATI, Nano 17). The entire setup was on top of a linear motorized stage that was able to travel horizontally towards or away from a sheet of plywood (500×1300 mm) acting as a vertical surface. The motor was powered by an ESC (Hakrc 40A 4-in-1) with the constant supplied voltage of 8.4 V.

In the experiments, a computer running Simulink Real-Time (MathWorks) with the data acquisition unit (NI PCI-6229) was employed for synchronization of the driving commands and measurements. The current consumed by the ESC was recorded through a Hall effect current sensor (LEM, GHS 10-SME). The motorized stage was controlled by a stepper motor (resolution: 25 μm) for varying the distance d from 1 to 400 mm at the increment of 1, 2, or 5 mm depending on d. At each distance, force and current measurements were taken at 2 kHz when the motor throttle was increased from 40% to
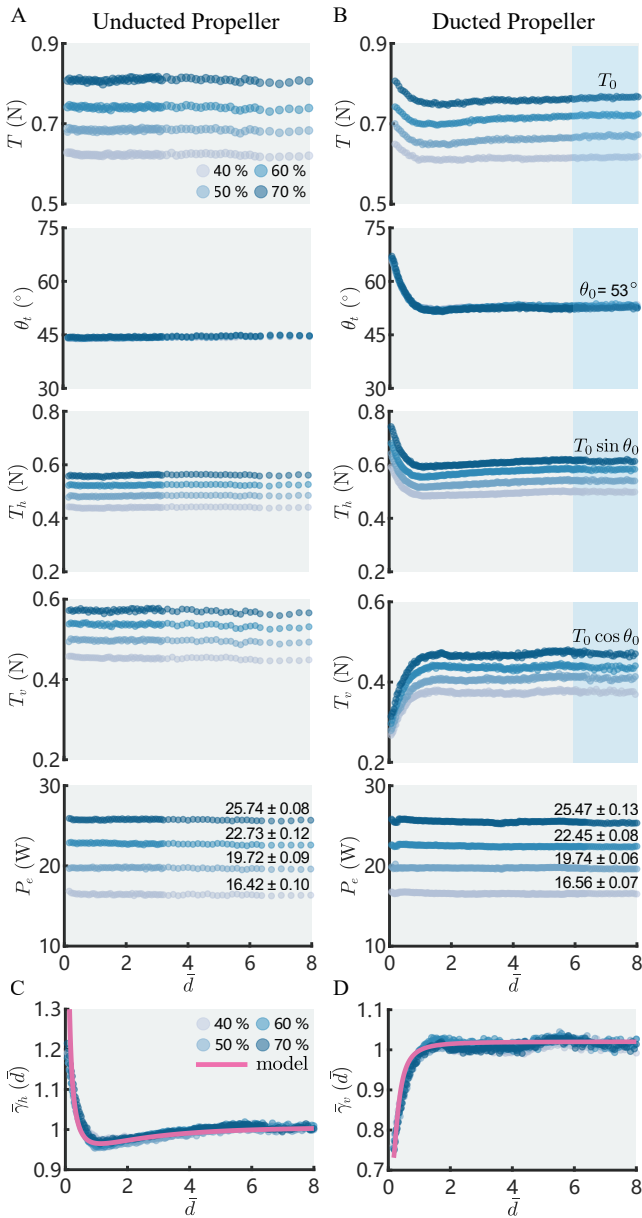
Fig. 4: Force and power measurement results. (A) Thrust and electrical power of the unducted propeller when it was subject to different commands by the ESC. (B) Thrust and electrical power of the ducted propeller when it was subject to different commands by the ESC. (C) Measurements and numerical model of the proposed coefficient for the horizontal component of the proximity effects, $\bar{\gamma}_h$. (D) Measurements and numerical model of the proposed coefficient for the vertical component of the proximity effects, $\bar{\gamma}_v$.

70%, at the increment of 10%. Each data point represents the average from the 10-s duration after allowing the system to reach a steady state for 20 s.

In addition to the tests outlined, the experiments were repeated with the same condition but without the duct. In this case, the results of the tilted propeller operating next to a vertical surface serve as benchmark measurements.

B. Thrust and Power Measurement Results

The measurements of thrust and electrical power are plotted against the normalized distance $\bar{d}$ in Fig. 4. First, it can be seen that for both cases (with and without the duct), the electrical powers remain constant for each thrust command.

This suggests that we can assume a constant command to the ESC leads to a constant electrical power, independent of $\bar{d}$. Next, focusing on the unducted propeller (Fig. 4A), the outcomes show no visible influence of the wall on the propelling thrust, even when d decreases to 1 mm. One possible interpretation of the observation is that, without the duct, the actuator disk stays normal to the propeller axis, and the thrust direction θ_t remains identical to θ_p regardless of $\bar{d}$.

On the other hand, the measurements from the ducted propeller reveal a significant variation with the wall distance. The duct dramatically amplifies the proximity effects. Overall, the magnitudes of the propelling thrusts do not change substantially compared to the unducted propeller when $\bar{d} > 4$. However, the thrust direction is markedly affected. As $\bar{d}$ is below four, there exists a drop in the vertical thrust and a rise in the horizontal force, corresponding to the increase in the angle θ_t. The change is more pronounced as $\bar{d}$ falls below one. The trend is consistent across four throttle commands.

C. Analysis and Empirical Models

To verify the MT-based model described by Eq. (8), the raw measurements of thrust elements from Fig. 4 are normalized by their respective values ($T_0 \sin \theta_0$ and $T_0 \cos \theta_0$) based on the fact that the electrical (and aerodynamic) power stays constant regardless of $\bar{d}$ for each motor command. To do so, $T_0 \sin \theta_0$ and $T_0 \cos \theta_0$ are calculated by averaging the force measurements taken when $\bar{d}$ is deemed sufficiently large ($6.0 \leq \bar{d} \leq 8.0$). The outcomes, equivalent to $\bar{\gamma}_h$ and $\bar{\gamma}_v$ from Eq. (8), show that the measurements from all four commands (and electrical powers) collapse together as evidenced in Fig. 4C and D. This validates the prediction from MT on the existence of $\bar{\gamma}_i$'s. Furthermore, since MT only describes $\bar{\gamma}_i$'s in terms of θ_t and θ_∞, which cannot be readily determined from MT alone (especially with the influence of the duct on the wake), we proposed empirical models for $\bar{\gamma}_i$'s based on the measurement data and the model derived to capture the ceiling effects in [18] as

$$\bar{\gamma}_h\left(\bar{d}\right) = \frac{1 + a_1\bar{d}^{-1} + a_2\bar{d}^{-2}}{\sqrt{1 + b_1\bar{d}^{-1} + b_2\bar{d}^{-2}}}, \quad \bar{\gamma}_v\left(\bar{d}\right) = \frac{1 + c_1\bar{d}^{-2}}{\sqrt{1 + d_1\bar{d}^{-2}}},$$
(10)

where a_i's, b_i's, c_1 and d_1 are to be numerically determined. Their values are likely dependent on the blade geometry and the profile of the duct. In this form, both $\bar{\gamma}_i$'s approach unity as $\bar{d} \to \infty$ as anticipated. The method of least squares produce $a_1 = 2.80, a_2 = 0.20, b_1 = 5.20, b_2 = 10.96, c_1 = 0.84 \times 10^{-2}$, and $d_1 = 6.49 \times 10^{-2}$ for the best fitted $\bar{\gamma}_h$ and $\bar{\gamma}_v$ with the R squared values of 0.91 and 0.90 respectively. The fitted results shown in Fig. 4C and D can be used to model the dynamics of the robot constructed from tilted and ducted propellers when it operates in near a vertical surface.

IV. ROTORCRAFT WITH TILTED AND DUCTED PROPELLERS

To leverage the findings on the proximity effects in the preceding section, a quadrotor with ducted and tilted propellers with a 2-fold rotational symmetry as presented in Fig. 1 and 5
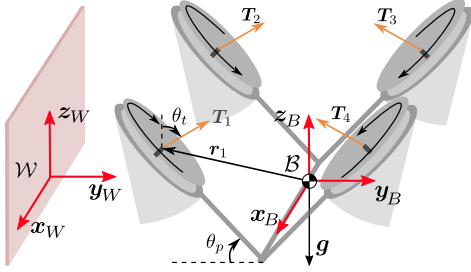
Fig. 5: Coordinate frames and robot configuration. The origin of the inertia frame $\mathcal{W}$ is located on the wall.

is proposed. In this section, we examine the hovering dynamics of the robot when the robot is in the vicinity of a vertical surface. Without direct sensing, we assume the flight controller does not compensate for the change in the propelling thrust induced by the wall. For simplicity, the surface is assumed approximately normal to the pitch axis of the robot.

A. Robot's Configuration and Coordinate Frames

As illustrated in Fig. 5, the proposed quadrotor with the body frame $\mathcal{B} = \{\boldsymbol{x}_B, \boldsymbol{y}_B, \boldsymbol{z}_B\}$ and mass m consists of ducted propellers that are tilted inwards about the roll axis $\boldsymbol{x}_B$. The robot is symmetrical about the $\boldsymbol{x}_B$-$\boldsymbol{z}_B$ plane except for the propeller directions. The tilted angle and the duct configurations are identical to the propeller tested earlier ($\theta_p = 45°$ and $\theta_d = 30°$). The inertial frame is defined as $\mathcal{W} = \{\boldsymbol{x}_W, \boldsymbol{y}_W, \boldsymbol{z}_W\}$, located on the wall with $\boldsymbol{y}_W$ being the surface normal. The position of the robot with respect to frame $\mathcal{W}$ is given by $\boldsymbol{p} = [x, y, z]^T$. The rotation matrix $\boldsymbol{R}$ relates the attitude of the body frame to the inertia frame.

B. Force and Torque Mapping

Prior to deriving the flight dynamics of the robot in the vicinity of a surface, we examine the force and torque produced by the robot. This deviates slightly from conventional vehicles due to the unique design and the proximity effects.

With four rotors, we let an the subscript i denote the ith propeller labeled in Fig. 5. The total thrust produced by the robot in its body frame is computed from Eq. (8) as

$$\boldsymbol{T} = \sum\nolimits_{i=1}^{4} \boldsymbol{T}_i = \sum\nolimits_{i=1}^{4} \left(\delta_i \bar{\gamma}_{h,i} \sin \theta_0 \boldsymbol{e}_2 + \bar{\gamma}_{v,i} \cos \theta_0 \boldsymbol{e}_3 \right) T_{0,i} \tag{11}$$

where $\boldsymbol{e}_j$'s are basis vectors and $\delta_i = 1$ for $i = 1, 2$ or $= -1$ for $i = 3, 4$. Meanwhile, the sum of torque in the body frame can be found from rotors' locations and spinning directions as

$$\boldsymbol{\tau} = \sum\nolimits_{i=1}^{4} \boldsymbol{r}_i \times \boldsymbol{T}_i + (-1)^{i+1} c_\tau \boldsymbol{T}_i \tag{12}$$

where $\boldsymbol{r}_i$ is a vector from the center of mass to the ith propeller and c_τ is the thrust-to-torque coefficient accounting for the propeller's drag. Remark that both Eqs. (11) and (12) assume the robot is approximately upright. This is essential in the current work as the fitted model of the proximity effects in the preceding section is only valid when θ_p is $45°$.

C. Flight Dynamics

To emphasize the impact of the wall, in this work, we limit the study to the cases where $\boldsymbol{y}_B$ lies approximately entirely

in the $\boldsymbol{y}_W$-$\boldsymbol{z}_W$ plane (orthogonal to the wall) and the vehicle operates near its hovering condition. This presumes the yaw angle of the robot is known and controlled. In this setting, the proximity effects are not only most pronounced but better understood as elucidated by the study in the preceding section.

Employing the roll-pitch-yaw (ϕ-θ-ψ) convention, the rotation matrix is $\boldsymbol{R}(\Theta)$ for $\Theta = [\phi, \theta, \psi]^T$. For small angles (the robot is close to upright) and angular rates, the linearized attitude dynamics of the robot is

$$\boldsymbol{J}\ddot{\Theta} = \boldsymbol{\tau}, \tag{13}$$

where $\boldsymbol{J}$ is the moment of inertia. Let g be the standard gravity, the translational dynamics of the robot follows

$$m\ddot{\boldsymbol{p}} = \boldsymbol{R}\boldsymbol{T} - mg\boldsymbol{e}_3. \tag{14}$$

Notice that this differs from a conventional quadrotor as the thrust does not necessarily align with the body axis $\boldsymbol{z}_B$.

V. PASSIVE WALL TRACKING STRATEGY

Herein, we demonstrate that, without a position controller, a simple method to regulate the roll angle would result in a wall tracking behavior of the robot. This is the consequence of the proximity effects on the horizontal and vertical thrust components produced by the propellers near the wall.

A. Attitude and Altitude Control

Focusing on the attitude (Θ) and altitude ($z = \boldsymbol{e}_3^T \boldsymbol{p}$) dynamics, Eqs. (13) and (14) are consolidated to

$$\begin{bmatrix} \boldsymbol{J}\ddot{\Theta} \\ m\ddot{z} + mg \end{bmatrix} = \begin{bmatrix} \boldsymbol{\tau} \\ \boldsymbol{e}_3^T \boldsymbol{R}\boldsymbol{T} \end{bmatrix}, \tag{15}$$

in which the input or the right hand side of Eq. (15) can be obtained from $T_{0,i}$'s via Eqs. (11) and (12):

$$\begin{bmatrix} \boldsymbol{\tau} \\ \boldsymbol{e}_3^T \boldsymbol{R}\boldsymbol{T} \end{bmatrix} = \sum_{i=1}^{4} \begin{bmatrix} \left([\boldsymbol{r}_i]_\times + (-1)^{i+1} c_\tau \boldsymbol{I}_{3\times 3} \right) \boldsymbol{t}_i \\ \boldsymbol{e}_3^T \boldsymbol{R}\boldsymbol{t}_i \end{bmatrix} T_{0,i}, \tag{16}$$

where $\boldsymbol{t}_i(\bar{d}) = \delta_i \bar{\gamma}_{h,i}(\bar{d}) \sin \theta_0 \boldsymbol{e}_2 + \bar{\gamma}_{v,i}(\bar{d}) \cos \theta_0 \boldsymbol{e}_3$ represents a vector thrust modifier, $[\boldsymbol{r}_i]_\times$ is the skew-symmetric matrix associated with $\boldsymbol{r}_i$, and $\boldsymbol{I}_{3\times 3}$ stands for an identity matrix. Defining a command input vector $\boldsymbol{T}_0 = [T_{0,1}, T_{0,2}, T_{0,3}, T_{0,4}]^T$, Eq. (16) can be re-written as $\boldsymbol{B}_{(\bar{d})} \boldsymbol{T}_0$ using a non-singular 4×4 matrix $\boldsymbol{B}$. As a consequence, we yield the combined dynamics equation for control:

$$\begin{bmatrix} \boldsymbol{J}\ddot{\Theta} \\ m\ddot{z} + mg \end{bmatrix} = \boldsymbol{B}_{(\bar{d})} \boldsymbol{T}_0. \tag{17}$$

Without the knowledge (or an estimate) of $\bar{d}$, we propose a PD control law that attempts to stabilize the robot to constant setpoints Θ_d (with $\psi_d = 0$ to maintain the presumed yaw angle) and z_d by assuming $\bar{d} \to \infty$ in the following form

$$\boldsymbol{T}_0 = \boldsymbol{B}_{(\bar{d} \to \infty)}^{-1} \begin{bmatrix} -\boldsymbol{K}_d \dot{\Theta} - \boldsymbol{K}_p (\Theta - \Theta_d) \\ mg - k_d \dot{z} - k_p (z - z_d) \end{bmatrix}. \tag{18}$$

where $\boldsymbol{K}_d$, $\boldsymbol{K}_p$, k_d, and k_p are (diagonal) positive gains. It can be seen that in the absence of the wall ($\bar{d} \to \infty$), the closed-loop dynamics constructed from combining Eqs. (17) and (18) are asymptotically stable. With a nearby surface, the results are discussed below.

TABLE I: Robot physical and control parameters

Var	Value	Unit	Var	Value	Unit
m	180	g	c_τ	3.3	cm
θ_0	53	deg	R	32	mm
$\boldsymbol{r}_1, \boldsymbol{r}_3$	$[\pm 5, \pm 7,5]^T$	cm	$\boldsymbol{r}_2, \boldsymbol{r}_4$	$[\mp 5, \pm 7,5]^T$	cm
k_p	13.5	Nm^{-1}	k_d	7.2	Nsm^{-1}
diag($\boldsymbol{K_p}$)	[16,18,4]	Ncmdeg^{-1}	diag($\boldsymbol{K_d}$)	[2,2,1]	Ncmsdeg^{-1}

B. Near-wall Response

To understand and leverage the closed-loop response of the robot, we begin by assuming that the direction of the wall is known and the yaw angle is well controlled ($\psi, \psi_d = 0$). In this setting (see Fig. 5), the wall only affects propellers 1 and 2. The pitch angle is irrelevant and can be separately stabilized to $\theta = 0$. Then, we presume that the combined attitude-altitude dynamics is substantially faster than the lateral dynamics as often assumed in the literature [14], [23].

1) Attitude-Altitude Response: With constant setpoints Θ_d and z_d, in this timescale, $\bar{d}$ (and, therefore, $\boldsymbol{B}_{(\bar{d})}$) is assumed approximately constant. After some algebraic manipulation, it can be shown that the PD controller prescribed by Eq. (18) shapes the attitude-altitude dynamics (Eq. (17)) into

$$\begin{bmatrix} \boldsymbol{J}\ddot{\boldsymbol{\Theta}} \\ m\ddot{z} \end{bmatrix} = \boldsymbol{B}_{(\bar{d})}\boldsymbol{B}_{(\bar{d}\to\infty)}^{-1} \left(-\boldsymbol{\kappa}_d \begin{bmatrix} \dot{\boldsymbol{\Theta}} \\ \dot{z} \end{bmatrix} - \boldsymbol{\kappa}_p \left(\begin{bmatrix} \boldsymbol{\Theta} \\ z \end{bmatrix} - \begin{bmatrix} \boldsymbol{\Theta}^* \\ z^* \end{bmatrix} \right) \right),$$

(19)

where $\boldsymbol{\kappa}_d = \text{diag}(\boldsymbol{K}_d, k_d)$, $\boldsymbol{\kappa}_p = \text{diag}(\boldsymbol{K}_p, k_p)$, and

$$\begin{bmatrix} \boldsymbol{\Theta}^* \\ z^* \end{bmatrix} = \begin{bmatrix} \boldsymbol{\Theta}_d \\ z_d \end{bmatrix} + \boldsymbol{\kappa}_p^{-1} \left(\boldsymbol{I}_{4\times 4} - \boldsymbol{B}_{(\bar{d}\to\infty)}\boldsymbol{B}_{(\bar{d})}^{-1} \right) \begin{bmatrix} \boldsymbol{0}_{3\times 1} \\ mg \end{bmatrix},$$

(20)

with $\boldsymbol{I}_{4\times 4}$ being an identity matrix. Under the condition that $\boldsymbol{B}_{(\bar{d})}\boldsymbol{B}_{(\bar{d}\to\infty)}^{-1}$ remains positive definite, it can be concluded that the PD control law asymptotically stabilizes the dynamics to the equilibrium state $(\boldsymbol{\Theta}^*, z^*)$ that is shifted from the setpoints $(\boldsymbol{\Theta}_d, z_d)$. The positive definite condition, which can be verified offline, is likely satisfied as long as $\boldsymbol{B}_{(\bar{d})}$ is sufficiently similar to $\boldsymbol{B}_{(\bar{d}\to\infty)}$.

Since the exact equilibrium state described by Eq. (20) depends on $\bar{d}$, the robot's configuration $\boldsymbol{B}$, and the controller gains, we numerically evaluate $\boldsymbol{\Theta}^*$ and z^* as a function of $\bar{d}$ (using parameters in Table. I). The outcomes are displayed in Fig. 6A and B. While the pitch angle θ^* remains unchanged from θ_d, the equilibrium roll angle ϕ^* is slightly larger than the setpoint ϕ_d when $\bar{d}$ is small. This corresponds to the robot tilting towards the wall due to the reduced vertical thrust component and increased horizontal force for the near-wall propellers as evidenced in the force measurements in Fig. 4. Similarly, the robot is expected to be in equilibrium at an altitude lower than the setpoint owing to the decreased vertical thrust as found in Fig. 4.

2) Lateral Position Response: Without position feedback, the lateral dynamics of the vehicle along $\boldsymbol{y}_W$ (dictating the wall distance $\bar{d}$) is not actively controlled. To inspect the lateral response with the timescale separation assumption, we apply the fact that $\boldsymbol{e}_2^T\ddot{\boldsymbol{p}} = \ddot{y}$ to the translational dynamics captured by Eq. (14) and compute $\boldsymbol{RT}$ from Eqs. (11) and (18) when
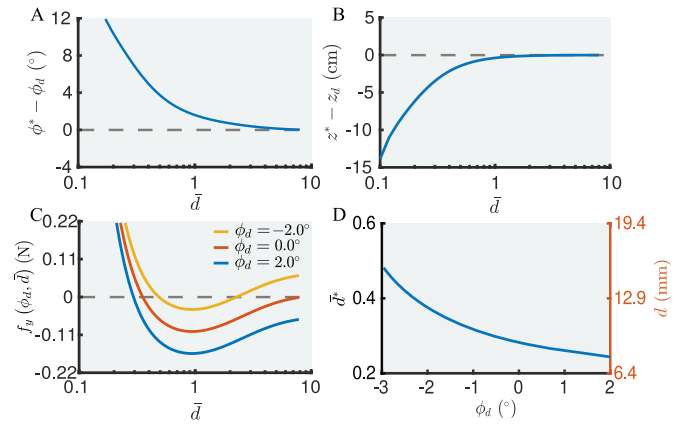

Fig. 6: Numerical predictions of the near-wall dynamics. (A) The expected stable roll angle when $\bar{d}$ is varied. (B) The expected stable altitude when $\bar{d}$ is varied. In (A) and (B), the lateral dynamics is not considered. (C) The lateral force f_y of the robot assuming the robot is in attitude equilibrium plotted as a function of $\bar{d}$. The plots show up to two equilibrium points for each ϕ_d. (D) The potentially stable equilibrium distance when $f_y = 0$ plotted as a function of the roll setpoint.

$\phi = \phi^*(\phi_d, \bar{d})$, $\theta, \psi = 0$, and $z = z^*(z_d, \bar{d})$. Denoting $\boldsymbol{e}_2^T\boldsymbol{RT}$ as $f_y(\phi_d, \bar{d})$, the lateral dynamics becomes

$$m\ddot{y} = f_y(\phi_d, \bar{d}).$$

(21)

The plot of $f_y(\phi_d, \bar{d})$ for the parameters listed in Table. I are shown in Fig. 6C. It can be seen that f_y effectively repels the vehicle from the surface ($f_y > 0$) at small distances. This is essentially explained by the growth in the horizontal thrust $\bar{\gamma}_h$ for the near-wall propellers (Fig. 6C). As $\bar{d}$ increases, there exist two equilibrium distances ($f_y = 0$), which can be manipulated through the roll setpoint ϕ_d as long as ϕ_d is sufficiently large. Based on the direction of f_y, the equilibrium point nearer to the wall (defined as $\bar{d}^*$) is potentially stable, in contrast to the second position. The profile of f_y around $\bar{d}^*$ is akin to a restoring force from a nonlinear spring. Through a suitable Lyapunov analysis around the equilibrium point $y = \bar{d}^*R$, it can be shown that the robot is locally stable at $\bar{d}^*$ as long as it is subject to sufficient $\dot{y}$-dependent damping (from air drag, for instance). Fig. 6D plots $\bar{d}^*$ against ϕ_d. This verifies that the equilibrium distance can be manipulated through the roll setpoint ϕ_d. Overall, the results in Fig. 6 are influenced by the physical and control parameters of the robot, but the trend is anticipated to carry over to other vehicles of similar sizes and configurations.

C. Wall Tracking Maneuver

Under the small-angle assumptions and the yaw angle control ($\psi \approx \psi_d = 0$), the translation of the robot in two horizontal directions is approximately decoupled. In the vicinity of a surface, the orthogonal distance is indirectly regulated through the roll setpoint. The robot remains free to traverse along the wall by altering the pitch setpoint. This forms the strategy for the passive wall tracking maneuver.

VI. FLIGHT EXPERIMENTS

In this section, we verify the near-wall behavior and wall-tracking strategy using the robot shown in Fig. 1. Several flight
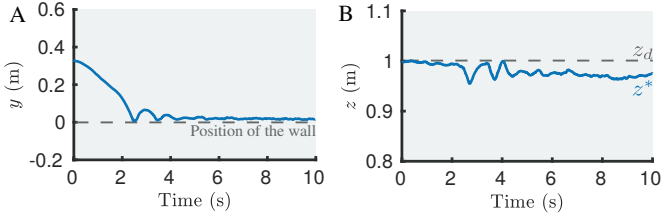
Fig. 7: Trajectory of the robot from the flight experiment with the final ϕ_d set to $0°$. (A) The distance of robot to the wall. The robot settled to the equilibrium distance just before $t = 3$ s. (B) Altitude of the robot. The robot dropped to ≈ 4 cm below z_d, consistent with the model's prediction.

experiments were carried out. The flight data are compared with the model predictions to validate the proposed methods.

A. Prototype and Experimental Setup

The robot was manufactured using identical components to the setup for the characterization experiment with the addition of a Crazyflie Bolt board, an airframe, and a two-cell LiPo battery. The robot weighs 180 g with a maximum vertical thrust of 280 g. A ground station computer running the Python scripts communicated with the Crazyflie Bolt through radio. The flight experiments were conducted in the motion capture (MOCAP) environment (OptiTrack) for the ground truth position and attitude measurements.

B. Near-wall Flights

1) Dependence on the roll setpoint: First, several flights were performed to demonstrate that, in proximity to a wall, the robot would stabilize to a nearby position with the varying gap size as the roll setpoint angle is altered.

To achieve this, a 50×50-cm sheet of plywood was adopted as a wall. The robot first was commanded, using the position feedback from the MOCAP to hover with the altitude of 1.0 m relatively far away from the wall ($\bar{d} \approx 12.5$ or $y \approx 0.4$ m). At time $t = 0$ s, the position controller along $\boldsymbol{y}_W$ (perpendicular to the wall) was disabled. The position control in the direction parallel to the wall, as well as the altitude, was retained to ensure the robot stays in the test volume. Simultaneously, ϕ_d was set to $2.0°$. This gently tilted and moved the robot towards the wall. After 3 s, ϕ_d was reset to $0°$ and the robot settled to the position $\bar{d}^* \approx 0.34$ (averaged over 10 s) from the wall as presented in the trajectory plots in Fig. 7. The flight record, of which a snapshot is shown in Fig. 8A, is available as the supplemental video. To validate the model of the closed-loop dynamics that describes the relationship between ϕ_d and $\bar{d}^*$, we repeated the flight experiments, but with the roll terminal setpoint ϕ_d set to different values after the robot hovered near the wall. Fig. 8A, 9A and B verify that the stable equilibrium positions shifts as a function of ϕ_d with the trend consistent with the model predictions. There exists minor differences in the values between the recorded distance and the model predictions, likely due to the linearization, inaccurate model parameters, and the validity of the proximity effect model when the vehicle is not perfectly upright. As seen in Fig. 8A, the robot stayed close to the wall even when ϕ_d was negative as predicted by Fig. 6C. This is because the actual roll angle $\phi \to \phi^*$ remained non-negative as shown in Fig. 8A.
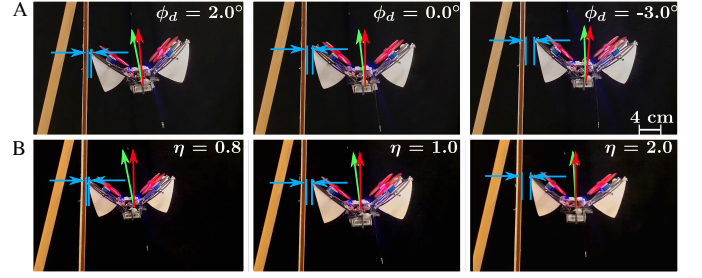

Fig. 8: Picture shows the flight experiment result. Green arrows indicated ϕ^*, red arrows indicated ϕ_d, and blue arrows highlight the gaps to the wall. (A) The equilibrium distance when ϕ_d is set from 2 ° to -3 °. (B) The attitude response when η is set from 0.8 to 2.0. The red arrow stands for ϕ_d and the green arrow stands for actual response ϕ.
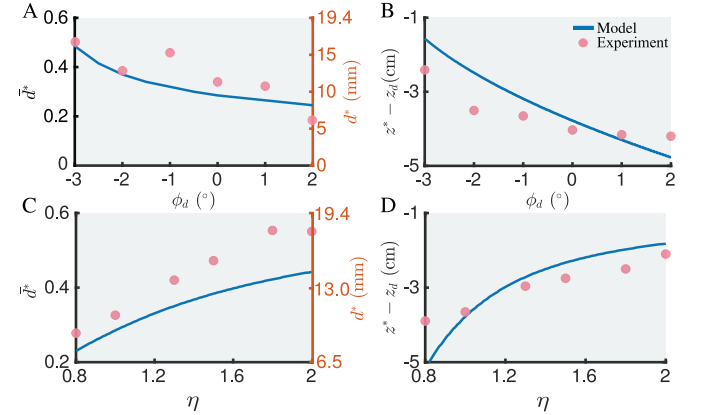

Fig. 9: Different equilibrium states according to various setpoints and controller gains. (A) Measured and predicted stable distances of the robot plotted against the roll setpoint. (B) Measured and predicted stable distances of the robot plotted against the gain factor η when $\phi_d = 0°$.

2) Influence of the control gain: Eq. (20) suggests that, in addition to ϕ_d, the first element of the gain $\boldsymbol{K}_p$, $K_{p,\phi}$, also influences the equilibrium state. Increasing the gain forces the actual roll angle to be closer to the setpoint, rendering the stable position to be further away from the wall. Hence, we introduce the dimensionless scaling parameter η such that $K_{p,\phi} \to \eta K_{p,\phi}$. An experiment similar to the previous set was carried out. In this test, when the robot was in the vicinity of the wall, the roll setpoint was reset to $0°$. Then, the tuning parameter η was varied from 0.8 to 2.0. The wall distance at each η value (averaged over 10 s) was recorded.

Example photos of the robot stabilized to different states corresponding to various values of η are shown in Fig. 8B. More quantitatively, Fig. 9C and Fig. 9D plot the stable equilibrium points $(\bar{d}^*, z^* - z_d)$ of the robot against η as found from the experiments. The outcomes match the trend predicted by the proposed model, confirming the effect of $K_{p,\phi}$ on the flight behavior in the near-wall setting.

C. Wall Tracking Flight

In this experiment, we staged a wall tracking demonstration to leverage the proximity effects in the application of the robot's navigation. This allows the robot to travel safely along a corridor in a visionless fashion.

The wall tracking flight was carried out in a corridor in the absence of the MOCAP. To regulate the altitude, feedback
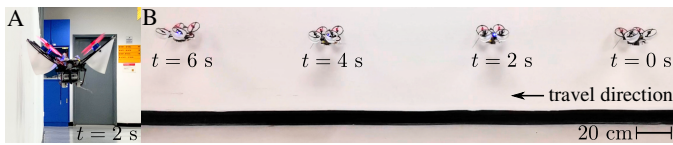
Fig. 10: Wall tracking flight performed in the corridor. (A) A front view of the robot showing a small gap between the vehicle and the wall. (B) A composite image demonstrating the robot traveling along the wall from right to left.

from a time-of-flight sensor (Crazyflie Flow Deck v2) was used for the altitude controller (Eq. (18)).

The flight began with the robot taking off in the middle of the corridor to the altitude setpoint $z_d = 0.5$ m. During the flight, the desired yaw angle ψ_d was minimized to zero, identical to earlier experiments. The same strategy was employed by a human pilot to fly the robot towards the wall. After reaching the equilibrium distance $\bar{d}^*$ at $t = 0$ s, the wall following was achieved by altering the pitch setpoint to $\theta_d = 4.0°$. As a result, the robot safely traveled over 3 m in 6 s before landing as shown in Fig. 10 and the supplementary video. Throughout the flight, the robot retained a small gap with the wall as an impactful collision was passively prevented by the aerodynamic repulsion. All in all, the experiment validates the effectiveness of the proposed wall tracking method.

VII. CONCLUSION AND DISCUSSION

In this work, we have re-designed a multirotor robot to leverage the fluid-structure interaction. The vehicle with ducted propellers strengthens the aerodynamic proximity effects when it operates in the vicinity of a vertical surface. Through momentum theory analysis and measurements, the aerodynamic forces were characterized. This enabled us to predict the flight dynamics of the robot near the wall. The outcome reveals that, without additional sensing or position feedback, there exists an equilibrium point where the robot hovers closely to the surface. The predicted behavior was thoroughly verified through a series of flight experiments, leading to a demonstration of a wall-tracking flight.

Despite the robot's ability to passively stay adjacent to the wall, the small angle approximation still limits the vehicle from realizing faster maneuvers. The major shortcoming of the current work is the requirement of a priori knowledge of the wall direction (equivalent to the yaw direction in this letter). Hence, possible improvements entail the estimation of the distance and direction of the wall based on IMU data and command inputs. Another pending question is whether the strategy is applicable to larger vehicles. Apart from the mass and inertia properties, the strength of the proximity effects may be highly scale-dependent as evidenced in [18]. Nevertheless, it is foreseeable that the capability to detect a wall would allow small robots with computational power too limited for comprehensive visual-inertial navigation systems to autonomously explore indoor or urban environments without any assistance from a human pilot. Potentially, this could play a crucial role in search and rescue operations where small robots are required to access confined spaces.

REFERENCES

[1] M. Petrlík, T. Báča, D. Heřt, M. Vrba, T. Krajník, and M. Saska, "A robust UAV system for operations in a constrained environment," *IEEE Robotics and Automation Letters*, vol. 5, no. 2, pp. 2169–2176, 2020.

[2] J. Scherer and B. Rinner, "Multi-UAV surveillance with minimum information idleness and latency constraints," *IEEE Robotics and Automation Letters*, vol. 5, no. 3, pp. 4812–4819, 2020.

[3] D. Falanga, K. Kleber, and D. Scaramuzza, "Dynamic obstacle avoidance for quadrotors with event cameras," *Science Robotics*, vol. 5, no. 40, 2020.

[4] K. McGuire, C. De Wagter, K. Tuyls, H. Kappen, and G. C. de Croon, "Minimal navigation solution for a swarm of tiny flying robots to explore an unknown environment," *Science Robotics*, vol. 4, no. 35, 2019.

[5] S. Tan, S. Zhong, and P. Chirarattananon, "A one-step visual-inertial ego-motion estimation using photometric feedback," *IEEE/ASME Transactions on Mechatronics*, pp. 1–1, 2021.

[6] S. Zhong and P. Chirarattananon, "An efficient iterated ekf-based direct visual-inertial odometry for mavs using a single plane primitive," *IEEE Robotics and Automation Letters*, vol. 6, no. 2, pp. 486–493, 2021.

[7] A. Briod, P. Kornatowski, J.-C. Zufferey, and D. Floreano, "A collision-resilient flying robot," *Journal of Field Robotics*, vol. 31, no. 4, pp. 496–509, 2014.

[8] P. Sareh, P. Chermprayong, M. Emmanuelli, H. Nadeem, and M. Kovac, "Rotorigami: A rotary origami protective system for robotic rotorcraft," *Science Robotics*, vol. 3, no. 22, 2018.

[9] C. J. Salaan, K. Tadakuma, Y. Okada, Y. Sakai, K. Ohno, and S. Tadokoro, "Development and experimental validation of aerial vehicle with passive rotating shell on each rotor," *IEEE Robotics and Automation Letters*, vol. 4, no. 3, pp. 2568–2575, 2019.

[10] Z. Liu and K. Karydis, "Toward impact-resilient quadrotor design, collision characterization and recovery control to sustain flight after collisions," in *2021 IEEE International Conference on Robotics and Automation (ICRA)*.   IEEE, 2021.

[11] S. Mintchev and D. Floreano, "A pocket sized foldable quadcopter for situational awareness and reconnaissance," in *2016 IEEE International Symposium on Safety, Security, and Rescue Robotics (SSRR)*.   Ieee, 2016, pp. 396–401.

[12] S. Mintchev, S. de Rivaz, and D. Floreano, "Insect-inspired mechanical resilience for multicopters," *IEEE Robotics and automation letters*, vol. 2, no. 3, pp. 1248–1255, 2017.

[13] J. Shu and P. Chirarattananon, "A quadrotor with an origami-inspired protective mechanism," *IEEE Robotics and Automation Letters*, vol. 4, no. 4, pp. 3820–3827, 2019.

[14] C. Powers, D. Mellinger, A. Kushleyev, B. Kothmann, and V. Kumar, "Influence of aerodynamics and proximity effects in quadrotor flight," in *Experimental robotics*.   Springer, 2013, pp. 289–302.

[15] C. D. McKinnon and A. P. Schoellig, "Estimating and reacting to forces and torques resulting from common aerodynamic disturbances acting on quadrotors," *Robotics and Autonomous Systems*, vol. 123, p. 103314, 2020.

[16] E. Davis and P. E. I. Pounds, "Passive position control of a quadrotor with ground effect interaction," *IEEE Robotics and Automation Letters*, vol. 1, no. 1, pp. 539–545, 2016.

[17] S. A. Conyers, "Empirical evaluation of ground, ceiling, and wall effect for small-scale rotorcraft," Ph.D. dissertation, University of Denver, 1 2019.

[18] Y. H. Hsiao and P. Chirarattananon, "Ceiling effects for hybrid aerial–surface locomotion of small rotorcraft," *IEEE/ASME Transactions on Mechatronics*, vol. 24, no. 5, pp. 2316–2327, 2019.

[19] A. E. Jimenez-Cano, P. J. Sanchez-Cuevas, P. Grau, A. Ollero, and G. Heredia, "Contact-based bridge inspection multirotors: Design, modeling, and control considering the ceiling effect," *IEEE Robotics and Automation Letters*, vol. 4, no. 4, pp. 3561–3568, 2019.

[20] V. Britcher and S. Bergbreiter, "Use of a MEMS differential pressure sensor to detect ground, ceiling, and walls on small quadrotors," *IEEE Robotics and Automation Letters*, vol. 6, no. 3, pp. 4568–4575, 2021.

[21] T. Nakata, N. Phillips, P. Simões, I. J. Russell, J. A. Cheney, S. M. Walker, and R. J. Bomphrey, "Aerodynamic imaging by mosquitoes inspires a surface detector for autonomous flying vehicles," *Science*, vol. 368, no. 6491, pp. 634–637, 2020.

[22] M. Sitti, "Physical intelligence as a new paradigm," *Extreme Mechanics Letters*, vol. 46, p. 101340, 2021.

[23] M. Bangura and R. Mahony, "Thrust control for multirotor aerial vehicles," *IEEE Transactions on Robotics*, vol. 33, no. 2, pp. 390–405, 2017.